Soft Matter

Size dependent droplet interfacial tension and surfactant transport in liquid-liquid systems, with applications in shipboard oily bilgewater emulsions

Journal:	*Soft Matter*
Manuscript ID	SM-ART-09-2019-001892.R1
Article Type:	Paper
Date Submitted by the Author:	02-Jan-2020
Complete List of Authors:	Chen, Yun; University of Minnesota, Department of Mechanical Engineering Dutcher, Cari; University of Minnesota, Department of Mechanical Engineering

ARTICLE

Size dependent droplet interfacial tension and surfactant transport in liquid-liquid systems, with applications in shipboard oily bilgewater emulsions

Received 00th January 20xx,
Accepted 00th January 20xx

DOI: 10.1039/x0xx00000x

Yun Chen and Cari S. Dutcher †

Many liquid-liquid emulsions, including shipboard oily bilge waters (oil-in-water) and water entrained in diesel fuels (water-in-oil), are chemically stabilized by surfactants and additives and require treatment to destabilize and separate. The interfacial tension (IFT) of surfactant-laden interfaces between the continuous and dispersed phase, as well as the size of the dispersed droplets, are significant factors in determining emulsion stability. In particular, the timescale associated with a dynamic change in IFT due to surfactant transport is indicative of how fast the emulsion will stabilize. In the present work, the dynamic IFT of droplets at micro-scale (~80 μm) and milli-scale (~2 mm) is measured with simulated bilgewaters with soluble surfactant systems. It is found that the IFT of micro-scale droplets decays faster than that of the milli-scale droplets due to smaller diffusion boundary layer thickness. The change in IFT was also studied for water-soluble surfactants added into the dispersed phase and continuous phase for both milli- and micro-scaled droplets. The results show that the IFT of micro-scale droplets decreases to the equilibrium value faster when the surfactant is in outer phase than in the inner phase, while the IFT does not change significantly for the milli-scale droplets. The observations are explained by the change in diffusion limited to kinetic limited surfactant transport. Finally, the surfactant diffusivities, adsorption and desorption rate constants are calculated using Langmuir's equation. The results presented here provide insight into the fundamental mechanism of the surfactant transport and helps improve mitigation strategies of oil-water emulsions.

Introduction

Interfacial tension (IFT) of droplets has been extensively studied, due to their importance in multiphase systems such as the pharmaceutical products, food manufacturing, diesel fuel filtration system and shipboard bilge water treatment. For instance, bilge water is oily wastewater (oil-in-water) found in the bottom chamber of ships, which generally contains fuels, oil, grease, detergents, and sea water[1–6]. Direct offshore discharge of the bilge water into seas and oceans with more than 15 mg/L oil will cause serious pollution to the environment, hence it is prohibited by the International Maritime Organization (IMO)[7] and onboard treatment is required to remove the oil prior to discharge. In general, the presence of surfactants in the detergents of the bilge water can reduce the IFT of oil droplets and limit their coalescence, which enhances the stability of the emulsion and increases the difficulty of those oil droplets removal[5,6]. This difficulty of removing droplets from the emulsion has also been observed in the diesel fuel filtration system. During transportation of the diesel fuel, small amount of water can enter the fuel oil which leads to the formation of water-in-fuel emulsions[8]. This entrained water can cause serious damage on the diesel-powered engines, such as corrosion and rust of the components[9,10]. Similar to the bilge water system, due to the existence of surfactant in diesel fuel, the water-in-fuel emulsion is stabilized with droplets ranging from 10 to 150 μm[10]. The surfactants in the emulsion lower the IFT of the water droplets, which decreases the droplets' ability to coalesce and making it difficult to be separated from the bulk.[8,11–13]

In general, when a droplet is formed in a solution with surfactant bulk concentration, C_∞, three simultaneous processes (adsorption, desorption, and diffusion) occur during the transport of surfactant molecules to the interface[12,14]. Driven by the entropic force, the molecules near the interface adsorb and desorb from the interface that leads to the depletion of surfactants in the region adjacent to the interface. The surfactant molecules in the bulk will then repopulate and diffuse to this region followed by the adsorption to the interface, which reduces the IFT of the droplets from its initial value, γ_0. After some time, the IFT reaches equilibrium to γ_{eq} as the number of surfactant molecules adsorbing to the interface is equal to the number desorbing, where the net concentration of molecules on the interface is constant (i.e., $\Gamma = \Gamma_{\mathrm{eq}}$). There are two parameters of this dynamic evolution of IFT that are of interest: the equilibrium IFT, γ_{eq}, and the time scale associated with the dynamic drop IFT, τ, to the equilibrium value. Both γ_{eq} and τ are affected by surfactant bulk concentration,

---

† Department of Mechanical Engineering, University of Minnesota, MN, 55455, USA
Email: cdutcher@umn.edu

Electronic Supplementary Information (ESI) available: [details of any supplementary information available should be included here]. See DOI: 10.1039/x0xx00000x

diffusivity of the molecules[15,16], type of surfactant, and bulk convection[17]. In addition, τ is also affected by the droplet size[8,12,14].

Seminal works have studied the timescales of the varied surfactant transport mechanisms on IFT. In particular, if the time scale of diffusion into the depletion region is greater than the time scale of adsorption, the dynamic IFT is diffusion controlled. On the other hand, if there is no instantaneous equilibrium of surfactant molecules between the interface and the vicinity, and the time scale for the adsorption is greater than that of the diffusion, the dynamic IFT is then kinetic controlled[16]. This kinetic controlled surfactant transport is due to the existence of adsorption and desorption energy barrier. Different models have been developed to describe the diffusion and kinetic adsorption of surfactant transport under various limit. Ward and Tordai first developed a model to predict the surfactant concentration at the interface for diffusion controlled surfactant transport[18]. This model is the basis of all contemporary models that describe the surfactant transport from the bulk to the depletion region. For kinetic controlled surfactant transport, the rate of the adsorption can be predicted by Langmuir model[15,19], which calculates the adsorption and desorption rate constants.

Beyond the Langmuir isotherm and the original Ward and Tordai model, more advanced models can be applied when interaction between the surfactant molecules are involved in more complex systems. Frumkin isotherm[20–22], for instance, has included a dimensionless parameter that accounts for the van der Waals forces between the hydrocarbon chains of the surfactant molecules as well as the repulsive force due to the head groups. The Frumkin isotherm can be reduced to Langmuir isotherm when this parameter is set to zero. Studies have shown that the equation of state with Frumkin isotherm fits better to the surface tension measurement of a homologous series of polyethoxylated surfactants than that with Langmuir isotherm[23], due to the better description of the interactions between surfactants.

Both Langmuir and Frumkin isotherm are classified as "pseudo-nonionic" model when the surface charge is ignored. When charge effects between the molecules are involved, "ionic" models need to be considered[20,24]. The Davies isotherm can be used to describe the equilibrium adsorption of ions from an ideal bulk solution to a charged surface that has no interacting ions. Particularly, the Davies isotherm relates the adsorbed surface concentration to the bulk concentration and surface potential. When surface potential is zero, Davies isotherm reduces to Langmuir isotherm. Datawani and Stebe[26] applied Davies adsorption isotherm to study the adsorption of a charged amphiphile at the interface. By using the Davis isotherm, they found good prediction of surface tension behavior of the anionic surfactant Aerosol-OT[25]. However, Davis model may be not sufficient in all cases due to lack of the consideration for interaction between molecules. Therefore, a combined Frumkin-Davies isotherm can include intra-monolayer interactions into the Davies isotherm[20], valid when the thickness of the electric double layer is of the order of the interfacial region. Borwankar and Wasan[27] has developed an adsorption model under the limit when the double layer thickness is much larger than the interfacial region, where excess surfactant concentration is considered to be the part of the aqueous phase. The electrostatic effects of the counterions at the air-water interface can then be incorporated in the model. Finally, recent works[28–30] have contributed to the models that consider mixture of ionic and nonionic surfactants. In particular, the work by Mulqueen and Blankschtein[28] has been shown good prediction for SDS and nonionic surfactant mixture. Their work[29] also leads to a generalized Ward and Tordai equation that can be used for surfactant mixtures.

In order to distinguish the surfactant transport between diffusion-controlled and kinetic-controlled transport, Jin et. al[12] developed a critical length scale for the droplet size, which is dependent on the diffusivity of the surfactant molecules, adsorption rate constant, and the maximum surface coverage. If the droplet size is much greater than this critical length scale, the surfactant transport is diffusion controlled, while if it is much less than this critical value, the transport is kinetic controlled.

Knowing the limit under which the surfactant transport occurs is of importance to determine the time scale of IFT. For instance, Alvarez et. al[14] developed a diffusion-limited time scale for a spherical drop and found that smaller droplets reach the equilibrium IFT faster than larger droplets. Their results suggest that the curvature of the droplets has a significant impact on surfactant transport under diffusion limit. More recently, Narayan et. al[8] showed experimentally that the decaying time scale of IFT is orders of magnitude smaller in micro-scale droplets compared to milli-scale droplets, which provides an obvious evidence of the impact of curvature on the surfactant transport. In another work by Alvarez et. al, they have shown that the diffusion time scale can also be reduced with bulk convection to decrease the diffusion boundary layer[17]. In addition, their results suggest that using a low Reynolds number flow in the bulk solution can lead to a transition from diffusion to kinetic controlled surfactant transport.

The soluble surfactants themselves can present either in the dispersive phase (i.e., inside the droplet) or the continuous phase (i.e., outside the droplet), also impacting the timescale of the transport mechanisms. Despite the seminal works studying the dynamic IFT affected by various parameters, most of the studies focus on the case that surfactants are only added in one phase[15,17,31,32]. Yeung et. al[33] added the surfactant in the oil phase and measured the equilibrium IFT of droplets for water-in-oil and oil-in-water, but they did not consider the time scale for the change in IFT. Due to its relevance and potential application in liquid-liquid separation applications, studying dynamic IFT to calculate surfactant transport timescales in varied phases across droplet sizes is needed.

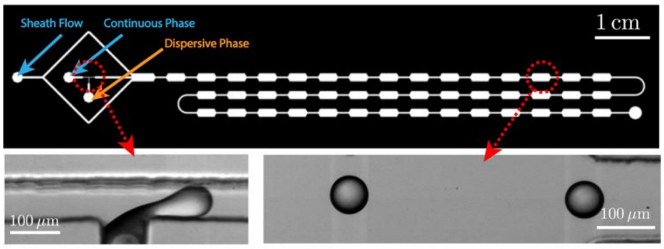

Fig.1 (Top) Microfluidic device for dynamic IFT measurement. (Bottom left) Image showing droplet generated at the T-junction. (Bottom right) Droplets enter the contraction and experience deformation.

The goal of this paper is to measure the dynamic IFT and calculate surfactant transport of both micro- and macro-scale droplets with the surfactants added to either dispersed or continuous. To simulate bilgewater, we use the simulated Navy Standard Bilge Mix (NSBM) #4 as the model oil mix (Table 1), which is a mixture of diesel fuel and lubrication oils, and synthetic sea water (SSW) as the aqueous phase. Two different surfactants are investigated in the current work. First is the detergent mix to simulate the surfactants in the bilge water (Table 1). The second is the Alcohol Ethoxy Sulfate (AES) as the model surfactant. Experiments are performed using microfluidics devices by adding the surfactant in SSW and compare the dynamic IFT for SSW as dispersive phase versus continuous phase. The results of this paper show for the first time that the IFT of the micro-scale droplets decays faster when the surfactant is in the continuous phase than that in the dispersive phase. However, under the same condition, the decaying time for milli-scale droplets does not change. The mechanism of phenomena is explained assuming both diffusion-limited and kinetic-limited surfactant transport. The surfactant diffusivity, adsorption and desorption rate are also obtained from the experiments to support our explanation.

Materials & methods

Chemicals. The chemicals used in this work simulate a bilge water emulsion system. The synthetic sea water (RICCA Chemical, CAT# 8363-5, $\rho = 1.023$ g/ml, $\mu = 1.88$ mPa $\cdot\, s$, ASTM D-1141, substitute ocean water without heavy metals) abbreviated as SSW, is used as the aqueous phase. The oil phase consists of Navy Standard Bilge Mix (NSBM) #4 (Naval Surface Warfare Center, Carderock Division, $\rho = 0.87$ g/ml, $\mu = 21$ mPa $\cdot$ s) abbreviated as the oil mix, of which the chemical components are listed in Table 1. The viscosity of the chemicals is measured by the magnetic bearing rheometer (AR-G2 TA Instrument). The surfactants used in this work are the simulated bilge detergent mix and model alcohol ethoxy sulfate (Stepan, STEOL CS-230) surfactant abbreviated as AES. The chemical compositions of the detergent mix are listed in Table 1, which is also used to simulate the detergents presented in the bilge water. The anionic surfactant AES is used as a model surfactant for the study of fundamental mechanism in the present work. Both surfactants are diluted in SSW with various concentration, as noted.

Table 1 Chemical Mixtures for Simulated

NSBM #4 Oil Mix	Detergent Mix
50% - Diesel Fuel Marine (MIL-PRF-16884N)	50% - Type 1 General Purpose Detergent (MIL-D-16791G(1))
25% - 2190 TEP Steam Lube Oil (MIL-PRF-17331K)	25% - Commercial Detergent Tide Ultra (liquid)
25% - 9250 Diesel Lube Oil (MIL-PRF-9000L)	25% - Degreasing Solvent (MIL-PRF-680C, Type III)

Using the detergent mix allows us to simulate the bilge water emulsions and study the IFT behavior in the navy environmental systems. However, since the detergent mix contains a number of different surfactants, a model surfactant, AES, is also used in order to more quantitatively estimate its transport mechanism. Each surfactant is added to the SSW phase with two different concentration. In particular, the comparison of dynamic IFT for SSW in the inner fluid and outer fluid for droplets of different sizes will be studied.

Pendant drop tensiometry. Each dynamic IFT measurement performed in the microfluidic device will be complemented by the

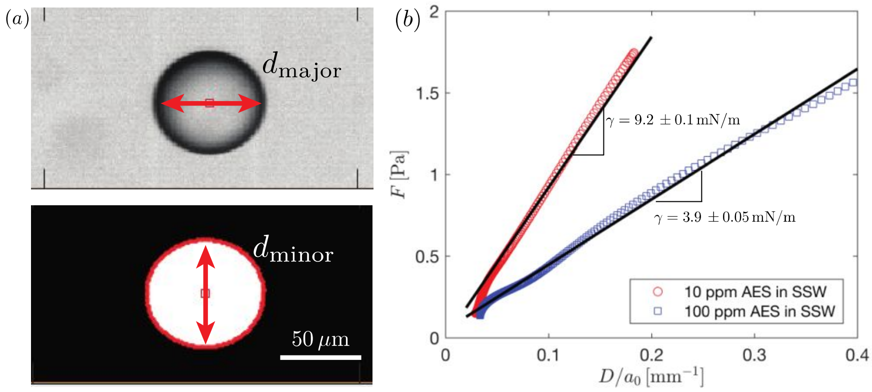

Fig. 2 (a) Droplet deformation at the contraction (b) Fitting of the experimental data of a droplet entering the contraction using Taylor's equation. The slope of the linear curve gives the interfacial tension of the droplets. F in this plot is defined as the terms on the left hand-side of Eq. (2).

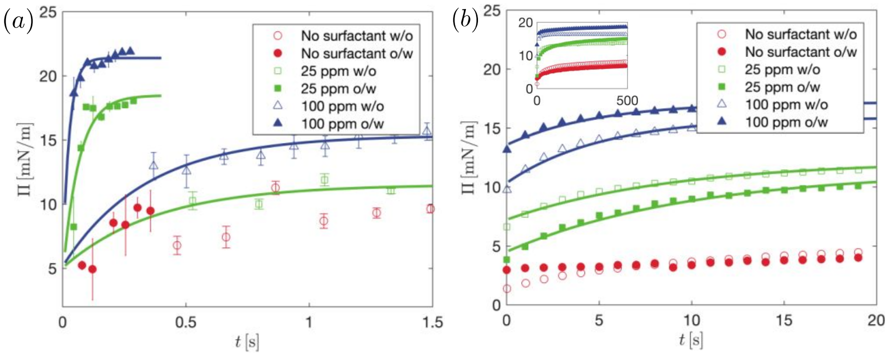

Fig. 3 Dynamic surface pressure of droplets with no surfactant, 25 ppm and 100 ppm detergent mix for water-in-oil (w/o) and oil-in-water (o/w) using (a) microfluidics tensiometry (~$75\mu\mathrm{m}$) and (b) pendant drop (~$2\ \mathrm{mm}$), respectively. The inset figure shows the surface pressure of a pendant drop over long-time scale. The decaying time scale, τ, of each experiment is extracted by fitting the $\Pi - t$ curve with the exponential function, $\Pi = \gamma_0 - (a\exp(-\mathrm{t}/\tau) + \mathrm{b})$, shown as the lines in the plot.

pendant drop tensiometry. The measurement is performed via a Drop Shape Analyzer (Kruss DSA30) using a syringe with dispersive phase fluid immersed in a cuvette containing continuous phase fluid. A droplet is formed at the needle tip and the droplet shape is analyzed using Young-Laplace fit to obtain time-dependent interfacial tension.

Microfluidic measurements. The design of the microfluidic device used for dynamic IFT measurement is shown in Fig. 1. The device includes three inlets for sheath flow phase, continuous phase, and dispersive phase. Same fluid will be injected through continuous phase and sheath flow phase in each experiment, while a different fluid for dispersive phase. This device uses a T-junction[34–38] to generate the droplet as shown in the bottom left figure in Fig. 1. Droplets generated at T-junction have a wide range of diameter depending on the ratio of pressure between the continuous and dispersive phase flow, and then flow downstream to the serpentine channel with a series of contraction chambers[8,15,39]. The speed and spacing of the droplets can be controlled by the sheath flow pressure.

The microfluidic device is fabricated using standard soft lithography technique[40–42]. In general, a silicon wafer is first cleaned using piranha solution and then spin coated with negative photoresist (SU-8 2050, Microchem). After the pre-bake, the wafer is then exposed under UV light with a mask aligner (Karl Suss) and then developed using acetate to form a mold of the design. The microfluidic channel is then made by pouring poly(dimethylsiloxane) (PDMS, Sylgard 184, Dow Corning) on the molded wafer and baking for 4 hours. The PDMS structure will then be cut from the wafer, followed by punching three inlets and an outlet are using a 1.2 mm OD biopsy punch (World Precision Instruments). It is then be bonded to a glass slide after an oxygen plasma treatment (Harrick Plasma). The device will be baked again for at least 2 hours before being used for the experiments.

For the experiments with oil mix as the continuous phase and SSW as the dispersive phase, we can use the procedure described in the previous section for making the PDMS device. However, as the PDMS is a hydrophobic material, hydrophilic treatment on PDMS is required to invert the liquid phases, as SSW is used as the continuous phase and oil mix as the dispersive phase to simulate the bilge water emulsion. Several works have studied the hydrophilic treatment of PDMS device[43–47]. The method of treatment used in this work is modified from Tan et.al[48] and has been optimized for best surface

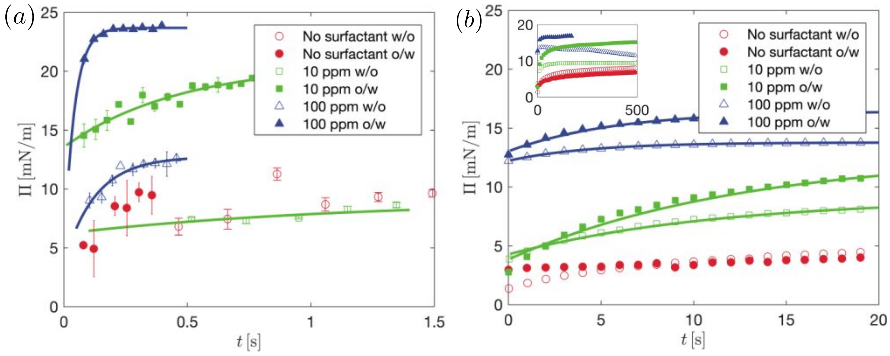

Fig. 4 Dynamic surface pressure of droplets with no surfactant, 10 ppm and 100 ppm AES for water-in-oil and oil-in-water using (a) microfluidics tensiometry (~$75\mu\mathrm{m}$) and (b) pendant drop (~$2\ \mathrm{mm}$), respectively. The inset figure shows the surface pressure of a pendant drop over long-time scale. The decaying time scale, τ, of each experiment is extracted by fitting the $\Pi - t$ curve with the exponential function, $\Pi = \gamma_0 - (a\exp(-\mathrm{t}/\tau) + \mathrm{b})$, shown as the lines in the plot.

treatment for the current devices: Before the PDMS is bonded to the glass slide from the regular process, the glass slide is first coated with a thin film of PDMS using the spin coater (WS-650, Laurell). After a second exposure to the oxygen plasma with 150 W for 15 minutes subject to oxygen flow at 300 sccm, the device is immediately stored in DI water under vacuum at least for 7 days. The test of the treated device shows that diesel oil mix droplets are successfully generated in continuous SSW phase and the device remains hydrophilic for over 4 hours, which is sufficient to run an experiment for dynamic IFT.

The pressure regulator valves (Marsh Bellofram Type 3110 Analog circuit card regulators) are used to control the pressures for each inlet flow, which can be adjusted through a National Instruments Analog Input/output device with a cDAQ-9174 chassis, NI 9264 AO module, and NI 9201 AI module. The velocity of the fluid is controlled via the pressure regulator such that the Peclet number Pe is of order 10^3. The Peclet number is given by[49] $Pe_{\text{ext}} = ru/D_{\text{C < CMC}}$, and $Pe_{\text{int}} = Pe_{\text{ext}}\hat{u}(2r/H)^2$ for external and internal flow of the droplets, respectively. Here, r is the radius of the droplet, u is the external flow velocity, $\hat{u}$ is scaling of the internal circulation velocity, and H is the channel height. In the current experiments, $H{\sim}140\mu\text{m}$ such that $2r/H{\sim}1$, and $\hat{u}$ is dependent on the channel aspect ratio w/H and $\hat{\eta}$ [50], which can be estimated as 0.5 for a droplet at the center of the channel.[51] Therefore, the Peclet number for external and internal convection are approximately in the same order of magnitude $Pe_{\text{int}} = 0.5\,Pe_{\text{ext}}{\sim}O(10^3)$. The fluid of each phase is stored in microfluidic reservoirs (Elveflow) and is pumped via polyethylene tubing (BD Intramedic PE tubing) and fittings (IDEX). The microfluidic device is placed on an inverted microscope (Olympus IX83) and the experiments are recorded using a high-speed camera (Photron Mini UX100) with a $10\times$ objective.

The experiments are recorded at frame rate from 25000 to 40000 fps and analyzed using custom particle-tracking code in MATLAB. The detected edge of the droplets entering a contraction is shown in Fig.2 (a). The diameter, average velocity, and the location of the droplets can be obtained via image analysis. This provides a useful tool for extracting the dynamic IFT from the current experiments. In general, when a droplet enters the microfluidic contraction channel, it deforms along the flow direction due to the external continuous phase flow. According to the study by Taylor[52], this deformation can be quantified in terms of a dimensionless parameter,

$$D(x) = \frac{d_{\text{major}}(x) - d_{\text{minor}}(x)}{d_{\text{major}}(x) + d_{\text{minor}}(x)} \qquad (1)$$

, where $d_{\text{major}}(x)$ and $d_{\text{minor}}(x)$ are the lengths of the major and minor axes of the deformed droplet indicated in Fig.2 (a), and x is the location of the droplet as detected from the experiments. Seminal works have contributed on the theoretical modelling on a deforming droplet[49,53–55]. One of the commonly used simplified equation is

$$\alpha\eta_c\left(\frac{5}{2\hat{\eta}+3}\dot{\varepsilon}(x) - u(x)\frac{\partial D(x)}{\partial x}\right) = \gamma\frac{D(x)}{a_0} \qquad (2)$$

, where $\alpha = (2\hat{\eta}+3)(19\hat{\eta}+16)/(40(\hat{\eta}+1))$, $\dot{\varepsilon}(x) = \partial u/\partial x$ is the extensional rate, a_0 is the diameter of an undeformed droplet, and the $\hat{\eta} = \eta_{\text{d}}/\eta_{\text{c}}$ is the ratio of the viscosity of the dispersive phase to that of the continuous phase. Eq. (2) is a force balance equation of a deforming droplet, applicable to small deformations of dilute unconfined droplets, where the first term on the left-hand side indicates the deforming force from the external flow and is balanced by the restoring force from the interfacial tension force on the right-hand side. The second term on the left-hand side of Eq. (2) indicates the material rate of change of droplet deformation. Through image analysis, we are able to obtain all the aforementioned parameters for each individual droplet entering the contraction as a function of x. The IFT, γ, is then obtained by fitting Eq. (2) to the linear portion of the experimental data as shown in Fig. 2(b) of two droplets entering the first contraction with two different surfactant concentration, which is equal to the slope of the curve. For simplification, the left-hand side of Eq. (2) plotted on y-axis in is labelled as F. The droplets deformation is recoded at a series number of contraction channels in each experiment, which allows us to obtain the IFT as a function of time using the microfluidic devices.

Experimental results

Dynamic IFT Measurements at the Macro- and Micro-scale. Dynamic surface pressure, $\Pi = \gamma_0 - \gamma$, of detergent mix in SSW is shown in Fig. 3. The increasing of Π indicates the decreasing of IFT, γ. For all the cases, the decaying dynamic IFT of nominal “no surfactant” condition suggests that the oil mix sample provided already contains some surfactants, likely due to the diesel fuels. After adding 25 ppm and 100 ppm detergent mix in the SSW, the equilibrium IFT decreases further with respect to the concentration, which clearly shows the effect on the IFT from the addition of surfactants. By comparing the results between (a) and (b) in Fig. 3, equilibrium IFT from microfluidics agrees with the measurement from pendant drop. However, all concentrations show a clear drop in IFT for a micro-scale droplet over only 2 seconds, while the IFT for milli-scale droplets decays over 10 seconds, showing a size-dependent decaying rate of dynamic IFT. More interestingly, when comparing the results of oil-in-water (o/w) and water-in-oil (w/o) in Fig. 3(a), we observe faster IFT decaying rate (within 1 second) for the experiments with oil mix droplet in SSW in micro-scale compared to SSW droplet in oil mix (within 2 seconds). In contrast, the IFT decaying rate for the pendant drop does not change too much when SSW is in the outer phase, which implies that this phase dependency of decaying rate is also affected by the droplet size. In addition, a lower IFT (higher Π) value is observed for 25 ppm and 100 ppm detergent mix in SSW for oil-in-water in Fig. 3(a) compared to corresponding surfactant condition in pendant drop measurement in Fig. 3(b). In general, the equilibrium IFT is dependent only on bulk surfactant concentration, indicating that the IFT for the oil-in-water pendant drop experiments have not yet reached their equilibrium value, evident by the increasing surface pressure even at 500 seconds shown in 3(b) subplot.

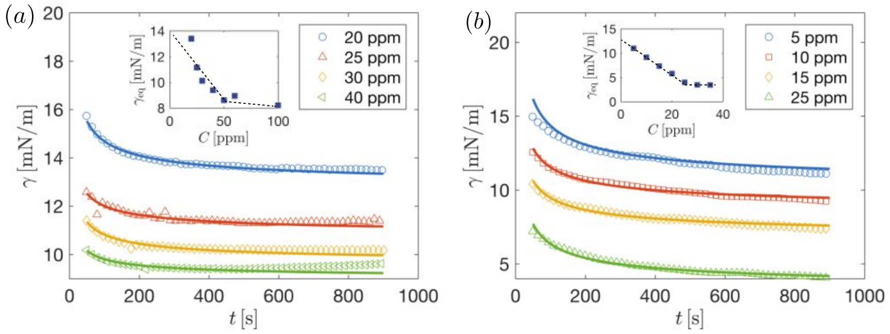

Fig. 5 Pendant drop measurement of dynamic IFT of diesel oil mix in SSW with (a) detergent mix and (b) AES at various concentration. The diffusivity, $D_{\mathrm{C}<\mathrm{CMC}}$, of each experiment is extracted by fitting the $\gamma - t$ curve with the function, $\gamma = \gamma_{\mathrm{eq}} + \lambda t^{-1/2}$, shown as the lines in the plot. The inset figures show the equilibrium IFT for each corresponding curve as a function of concentration, C, which gives the CMC of each surfactant.

Similar to the results using detergent mix, the IFT decays faster for micro-scale droplets compared to milli-scale droplets using AES as shown in Fig 4. In addition, Fig. 4 (a) also shows faster IFT decaying rate (within 1 second) when SSW is in the outer phase (within 2 seconds). This provides the evidence that the size and phase dependency of decaying rate is not unique for detergent mix, but a more general phenomenon for different surfactants in the current liquid-liquid system. We will explain the fundamental mechanism of this decaying rate difference in “Discussion” section. For the pendant drop measurements, however, the IFT starts increasing significantly after the initial sharp decrease for 100 ppm AES in SSW in the inset of Fig. 4 (b), while the IFT of 10 ppm AES in SSW increases with a small amount. The results here are different from Fig. 3 (b), in which no significant increase of IFT is observed for detergent mix. The AES used in the current study has carbon chain length from 10 to 16, while the octanol-water partition coefficient, Kow, of AES increases from 0.95 to 3.9 with carbon chain length ranges from 12-18[56]. Therefore, it is possible that AES has some solubility in oil mix, and the molecules will desorb from the interface into the oil phase at a longer time scale after they first transport from the water phase to the interface, which results in the increase of IFT. In addition, the oil phase in our system is the oil mix that contains mixture of chemicals, which may further increase the possibility that leads to high solubility of AES in the oil phase.

Table 2 Surfactant parameters obtained from pendant drop tensiometry for

Surfactant	**Detergent Mix**	**AES**
$\boldsymbol{M_{\mathrm{w}}}$ $(\mathbf{g/mol})$	300	420
$\boldsymbol{\Gamma_{\infty}}$ $(\mathbf{mol/m^2})$	1.52×10^{-6}	2.53×10^{-6}
$\boldsymbol{\kappa}$ $(\mathbf{m^3/mol})$	380	904
$\mathbf{CMC}$ $(\mathbf{mol/m^3})$	1.77×10^{-1} (50 ppm)	6.25×10^{-2} (25 ppm)
$\boldsymbol{D_{\mathrm{C}<\mathrm{CMC}}}$ $(\mathbf{m^2/s})$	3.19×10^{-11}	1.9×10^{-10}

Characterization of Surfactant Properties. To understand the fundamental mechanism of the surfactant transport based on our experimental observation, the surfactant parameters, such as the critical micelle concentration (CMC), maximum surfactant surface coverage, Γ_{∞}, Langmuir constant, κ, and the diffusivity of the surfactant molecules below CMC, $D_{\mathrm{C}<\mathrm{CMC}}$ needs to be obtained first. To find CMC, a series of pendant drop experiments are performed to measure the dynamic IFT with surfactant concentration varying from 5 to 60 ppm for both detergent mix and AES as shown in Fig. 5.

One commonly used diffusion equation when IFT approaches equilibrium derived by Ward and Tordai is[18]

$$\gamma - \gamma_{\mathrm{eq}} \sim \frac{RT{\Gamma_{\mathrm{eq}}}^2}{C}\sqrt{\frac{\pi}{4D_s t}} = \lambda t^{-\frac{1}{2}}, \qquad (3)$$

where γ_{eq} and Γ_{eq} are the equilibrium IFT and surfactant concentration at the interface, respectively. Here, R is the gas constant, T is the ambient temperature, C is the surfactant concentration of the bulk, and D_s is the surfactant diffusivity. By fitting Eq. (3) to the experimental data in Fig. 5 (a) and (b) we can first extract γ_{eq} as well as the value of λ for each curve, which is plotted as a function of C in the inset figures. The CMC of each surfactant in SSW can be directly obtained, which is approximately 50 ppm and 30 ppm for detergent mix and AES, respectively. Next, the Gibbs adsorption energy equation is applied and fitted to the linear portion of $\gamma_{\mathrm{eq}} - C$ plot, when C is close to CMC[16,19] to obtain Γ_{∞},

$$\Gamma_{\infty} = -\frac{1}{nRT}\left(\frac{\partial \gamma}{\partial \ln C}\right)_T, \qquad (4)$$

where $n = 2$ for anionic surfactant. After Γ_{∞} is obtained for each surfactant, Langmuir isotherm is then applied to obtain the equation of state[57–59]

$$\frac{\Gamma_{eq}}{\Gamma_{\infty}} = \frac{\kappa C}{1+\kappa C} \qquad (5)$$

$$\gamma = \gamma_0 + nRT\Gamma_{\infty}\ln\left(1 - \frac{\kappa C}{1+\kappa C}\right) \qquad (6)$$

, where γ_0 is the initial IFT of the system. Eq. (6) is fitted again with $\gamma_{\mathrm{eq}} - C$ plot to obtain the value of κ of each surfactant. The Langmuir constant, κ, indicates the affinity of the surfactant molecules for the interface[12,15]. Finally, Eq. (3) and (5) are combined to obtain the diffusivity of the surfactant, $D_{\mathrm{C}<\mathrm{CMC}}$, in the current experiments below CMC ,

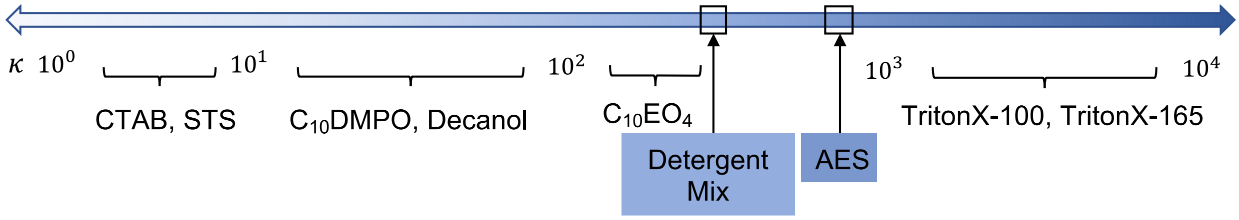

Fig. 6 Comparison of κ for detergent mix and AES with other commonly used surfactants. The larger the κ, the more active the surfactant will reduce the interfacial tension.

$$D_{\mathrm{C<CMC}} = \left[\frac{RT\Gamma_{\infty}{}^{2}\kappa^{2}C\pi^{1/2}}{2(1+\kappa C)^{2}\lambda}\right]^{2}. \qquad (7)$$

The extracted values are listed in Table 2. Since the detergent mix contains various types of surfactant such that it is difficult to obtain the exact value of molecular weight. Therefore, an approximate value of molecular weight of 300 g/mol for the detergent mix is assumed in the current system based on the average value of its surfactants. The extracted value of Γ_∞ , κ for both surfactants are all reasonable and within the range of typical surfactants[15,60]. The diffusivity, $D_{\mathrm{C<CMC}}$, is extracted using Eq. (7) by fitting Eq.(3) to the data as shown in Fig. 5 (a) and (b). $D_{\mathrm{C<CMC}}$ of AES extracted here are within the same order of magnitude of typical value ($\sim 10^{-10}$) for nanometer sized molecules, while the diffusivity of detergent mix is one order of magnitude smaller ($\sim 10^{-11}$). Two possible reasons could lead to this smaller value: first, the assumed value of the molecular weight of detergent mix may not be accurate due to the mixture of the various types of surfactant molecules in the systems; second, the existence of different types of surfactant molecules may also affect each other when transporting or adsorbing to the interface.

Discussion

Based on the results in Fig. 6 and Table S1, we found that the surface maximum concentration, Γ_∞, of the surfactant used in the current study are within the same order of those surfactants in the literature. This is standard for most surfactants; it is common to see values on the order of 10^{-6} m^2/mol with little variation. In contrast, the Langmuir constant, κ, varies from 10^{-3} to 10^{7} m^3/mol [61]. The values of detergent mix and AES, near that of non-ionic $C_{10}EO_4$ and TritonX-100, provide an insight into the relative surfactant activity during transport to the interface and therefore the ability to reduce the interfacial tension.

In general, the surfactant transport in the bulk solution involves both diffusion and kinetic adsorption into the interface. Depending on the time scale of each process, if the diffusion time scale is larger than the adsorption time scale, then the transport is defined as *diffusion-controlled.* Otherwise, it is defined as *kinetic-controlled.* According to seminal theoretical work, the critical length scale for the droplet diameter, R_{C}, to distinguish the *diffusion-controlled* and *kinetic-controlled* transport for typical surfactants is estimated to be the order of $10\ \mu\mathrm{m}$[12]. In the current work, the size of a pendant drop is approximately $2\ \mathrm{mm}$, which is much larger than this R_C and can be considered as *diffusion-controlled.* The average droplet radius of the microfluidic experiments is around $40\ \mu\mathrm{m}$, which is in the same order of R_{C}. In this line of thought, we consider the surfactant transport for the microfluidic case as *mixed diffusion-kinetic-controlled.* This suggests that the time scale of diffusion and kinetic adsorption should also be in the same order of magnitude, and both diffusion and kinetic adsorption can affect the decaying IFT.

Diffusion Boundary Layer. The length scale across which the diffusion occurs needs to be defined in order to obtain a time scale for the diffusion of surfactants. From the work by Alvarez et al.[11,14], they equate the number of molecules on an interface at equilibrium to the number of molecules available in the volume nearby and obtain a depletion length, which is defined as the diffusion length scale. This can be expressed as $\Gamma_{\mathrm{eq}}A_{\mathrm{s}} = C_{\mathrm{bulk}}V_{\mathrm{s}}$, where A_{s} and V_{s} are the surface area and volume of the depletion depth near the interface of the droplet, respectively. Alvarez et al. obtained a diffusion length for a spherical geometry when the surfactant appears outside the droplet[14]. In the present work, this mass balance is applied in the current system for surfactant transport as shown in the schematics in Fig. 6(a). r is defined as the radius of the droplet, h_{si} and h_{so} are the diffusion length scale for the surfactant inside and outside the droplet, which can be expressed as

Table 3 Time scale of dynamic IFT extracted from pendant drop and microfluidic

	Pendant Drop				Microfluidics			
Surfactant	**Detergent Mix**		**AES**		**Detergent Mix**		**AES**	
C $(\mathrm{mol/m^3})$	0.0887 (25 ppm)	0.354 (100 ppm)	0.025 (10 ppm)	0.25 (100 ppm)	0.0887 (25 ppm)	0.354 (100 ppm)	0.025 (10 ppm)	0.25 (100 ppm)
$\tau_{\mathrm{in\_exp}}$ (s)	14.17	5.29	11.97	4.45	0.378	0.24	0.17	0.09
$\tau_{\mathrm{out\_exp}}$ (s)	16.15	6.85	14.41	5.82	0.065	0.027	0.06	0.03

$$h_{\mathrm{si}} = r\left[1-\left(1-\frac{3h_{\mathrm{p}}}{r}\right)^{1/3}\right],\ \text{if}\ \frac{3h_{\mathrm{p}}}{r}<1 \qquad (8)$$

$$h_{\mathrm{si}} = r, \qquad \text{if}\ \frac{3h_{\mathrm{p}}}{r}\geq 1 \qquad (9)$$

$$h_{\mathrm{so}} = r\left[\left(\frac{3h_{\mathrm{p}}}{r}+1\right)^{1/3}-1\right], \qquad (10)$$

where $h_{\mathrm{p}} = \Gamma_{\mathrm{eq}}/C_{\mathrm{bulk}}$ is the diffusion length for a planar interface[12,14]. In particular, the equations for h_{si} present two different expression which is limited by the value of r. If the radius of the droplet is large enough such that $r > 3h_{\mathrm{p}}$, then Eq. (8) is used to obtain h_{si} and it is a function of both r and h_{p}. However, when $r \leq 3h_{\mathrm{p}}$, then h_{si} is simply equal to r as shown in Eq. (9). Therefore, we define a critical radius $r_{\mathrm{c}} = 3h_{\mathrm{p}}$ based on the scaling analysis below which the predicted diffusion length from Eq. (8) is even greater than r, such that every space inside the droplet can be considered as the depletion region. Here, the prefactor “3” in the critical radius considers the geometric change of the diffusion boundary layer from a planar interface to a spherical interface. The ratio of the time scale between the surfactant transport in inner and outer fluid can be obtained by [12]

$$\tau_{\mathrm{in}}/\tau_{\mathrm{out}} \sim \left(h_{\mathrm{si}}/h_{\mathrm{so}}\right)^{3/2} \qquad (11)$$

The results of Eq. (11) are plotted in Fig. 6(b) and (c) at different concentration of detergent mix and AES, respectively. First, when the diameter of the droplets, D, is greater than $1\ \mathrm{mm}$, $\tau_{\mathrm{in}}/\tau_{\mathrm{out}}$ is asymptotically approaching 1 for any concentration. This can be understood in the situation when $r \rightarrow \infty$, the spherical interface is close to a planar surface such that the diffusion length scale for the inner and outer fluid would be the same. Similarly, when the concentration increases for both surfactants, the curves start shifting to the left, leading to the $\tau_{\mathrm{in}}/\tau_{\mathrm{out}}$ decreasing asymptotically to 1 for a fixed droplet size. This suggests that when the bulk concentration, C_{bulk}, increases, there are more amount of surfactant molecules provided to the interface, which as a result reduces the depletion length near the interface.

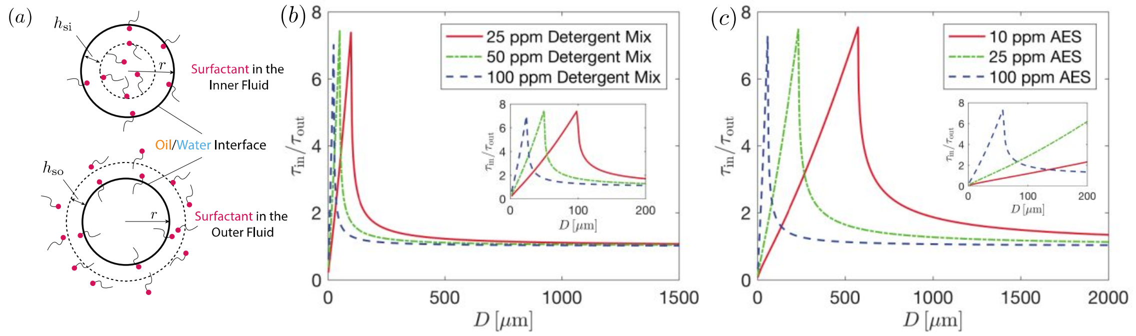

Fig. 7 (a) Schematic shows the surfactant transport inside and outside the droplets. Theoretical prediction of the ratio of the diffusion time scale, $\tau_{\mathrm{in}}/\tau_{\mathrm{out}}$, for surfactant transport between inner and outer fluid as a function of droplet diameter for various concentration of (b) detergent mix and (c) AES. Inset figures show the ratio of diffusion time scale for micro-scale droplets.

Next, when D decreases below $1\ \mathrm{mm}$, $\tau_{\mathrm{in}}/\tau_{\mathrm{out}}$ starts increasing until it reaches a maximum value at the critical radius $r_{\mathrm{c}} = 3\mathrm{h}_{\mathrm{p}}$, suggesting an increasing inner boundary layer length compared to the outer layer. However, when D further decreases to be smaller than $2r_{\mathrm{c}}$, $\tau_{\mathrm{in}}/\tau_{\mathrm{out}}$ starts decreasing again. The size of the micro-scale droplets in our current experiments falls in the range when this transition occurs. In order to further validate the prediction of $\tau_{\mathrm{in}}/\tau_{\mathrm{out}}$ from the analytical equations and investigate the mechanism of the surfactant transport, the decaying time scale of the dynamic IFT from the experiments shown in Fig. 3 and Fig. 4 are extracted as listed in Table 3.

The predicted $\tau_{\mathrm{in}}/\tau_{\mathrm{out}}$ for pendant drop ($\sim 2\ \mathrm{mm}$) agrees with the experiments that diffusion time scale of surfactants transport in inner and outer fluid are the same. However, the predicted $\tau_{\mathrm{in}}/\tau_{\mathrm{out}}$ does not work well with the results of micro-scale droplets ($\sim 75 \mu\mathrm{m}$) from the experiments. One possible reason that will cause this disagreement between the experiments and prediction is due to the surfactant transport affected by the kinetic-controlled surfactant adsorption, since the size of the droplets in the current microfluidics experiments is in the same order of magnitude of R_{C} as mentioned in the previous section. Moreover, the microfluidics experiments are subject to continuous phase flow which induces convection inside and outside the droplet. The Peclet number in the current experiments is $Pe \sim \mathrm{O}(10^3)$ for both inside and outside the droplets as mentioned in the previous section, which further suggests that the surfactant transport is kinetic-controlled for both inside and outside the droplet[15].

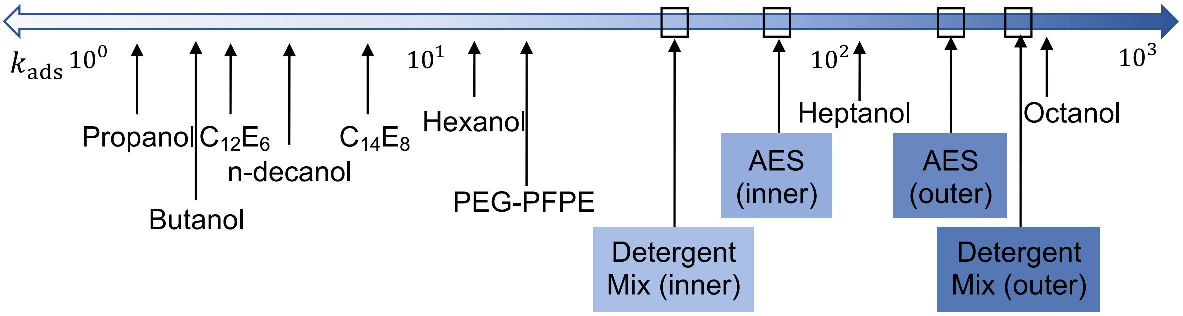

Fig. 8 Comparison of adsorption rate constant, k_{ads}, of detergent mix and AES for both surfactant in inner and outer phase of concentration below CMC.

Adsorption and Desorption Rate Constant. For kinetic-controlled surfactant transport, the adsorption rate, k_{ads}, and desorption rate, k_{des} governs the time scale of the surfactant transport, which can be obtained from Langmuir's equation[15,57],

$$\frac{\Gamma(t)}{\Gamma_\infty} = \frac{\Gamma_{\mathrm{eq}}}{\Gamma_\infty}(1 - \exp(-t/\tau_s)) \qquad (12)$$

With Eq. (12), the equation of state for dynamic IFT can be obtained as

$$\gamma(t) = \gamma_0 + nRT\Gamma_\infty \ln\left(1 - \frac{\Gamma_{\mathrm{eq}}}{\Gamma_\infty}(1 - \exp(-t/\tau_s))\right) \qquad (13)$$

The constant, τ_s, is obtained by fitting Eq. (13) to the experiments and can be related to adsorption and desorption rate constant as [15],

$$\tau_s = \frac{1}{k_{\mathrm{des}}}\frac{1}{1+\kappa C}, \qquad (14)$$

where $\kappa = k_{\mathrm{ads}}/k_{\mathrm{des}}$. The extracted value of k_{ads} and k_{des} from microfluidics experiments are listed in Table 4. The values of k_{ads} for all the cases extracted are within the reasonable range of order of magnitude $10^0 \sim 10^2\ \mathrm{m^3/mol\cdot s}$ for typical surfactants[12,57,60]. As shown in Fig.8 and Table S1, the adsorption rate constant, k_{ads}, calculated values of both detergent mix and AES are also within the broad range of values reported for other surfactants, near that of heptanol and octanol. These values are higher than most of the surfactants reported in the literatures, which is generally around or below 10^1.

Clearly, the adsorption rate is smaller when the surfactant is inside the droplet, suggesting larger energy barrier for the surfactant molecules. Several possible cases can be considered for this adsorption barrier, as described by Eastoe and Dalton[19]. The most likely case is that the molecules need to be in the correct orientation for adsorption. If the molecule experiences steric hindrances preventing the ideal orientation needed to adsorb, it will prefer to diffuse back to the bulk to rearrange itself than reach the adsorbed state. For the study here, when the surfactant is in the inner phase, the concaved orientation may result in the sterically suppressed adsorption rate.

In general, the adsorption rate is independent of surfactant concentration below CMC. However, it does have a CMC dependence. The results in Table indicates two concentration for each surfactant, one is above the CMC and the other is below CMC. Above CMC, the demicellization[62,63] process of those micelles that occurs before the surfactant molecules adsorbed onto the interface will affect the time scale of the kinetic adsorption. In particular, the decrease in adsorption rate is much greater for detergent mix when surfactant concentration is above CMC, which may be due to a mixture of micelles that form more appreciably affecting the surfactant adsorption.

The results of the impact of interfacial curvature on the decaying timescale found here is applicable to both simple and complex systems. Based on the scaling analysis, $\tau_{\mathrm{in}}/\ \tau_{\mathrm{out}}$ is strongly dependent on the size of the droplet for both the complex detergent mix and simple model surfactant AES. The phase dependency of the decaying time scale of IFT becomes increasing pronounced as the droplet size decreases. The results shown here may have potential application to explain broader soluble surfactant-driven emulsion phenomena, such as spontaneous emulsification[64], which involves soluble

Table 4 Surfactant adsorption and desorption rate obtained from microfluidic experiments for detergent mix and AES

Surfactant		Detergent Mix		AES	
C $(\mathrm{mol/m^3})$		0.0887 (25 ppm)	0.354 (100 ppm)	0.025 (10 ppm)	0.25 (100 ppm)
$k_{\mathrm{ads}}\ (\mathrm{m^3/mol\cdot s})$	Inner	54.5	5.6	95.2	88.2
$k_{\mathrm{des}}\ (1/\mathrm{s})$		0.14	0.02	0.11	0.09
$k_{\mathrm{ads}}\ (\mathrm{m^3/mol\cdot s})$	Outer	299.1	96.2	220.7	170.9
$k_{\mathrm{des}}\ (1/\mathrm{s})$		0.78	0.25	0.24	0.19

surfactant transport at and even across curved liquid-liquid interfaces.

Conclusions

In the present work, the time scale associated with surfactant transport and its impact on the dynamic IFT of droplets are studied. The IFT of the droplets is a significant factor for the emulsion stability in a variety of liquid-liquid systems including the bilgewater and diesel fuels. To understand the different mechanism of surfactant transport to an interface, we study changes in IFT as a function of droplet size and phase. Dynamic IFT for droplets micro-scale micron-scale (~80 μm) and milli-scale (~2 mm), with two different surfactants, simulated bilge detergent mix and AES, are measured. The results of IFT are also compared by adding the surfactant into the aqueous phase under both oil-in-water and water-in-oil conditions. The current results show that, for both surfactants, IFT decays faster for micro-scale droplets (~1 s) than milli-scale droplets (~10 s). This is because smaller droplet size leads to a smaller diffusion boundary layer thickness, which reduces the time it takes for the surfactant molecules to diffuse to the depletion region from the bulk. In addition, for micro-scale droplets, the IFT decays faster if the surfactant is in outer phase than in the inner phase. In contrast, the IFT decaying rate does not depend on the phase to which the surfactant is added for milli-scale droplets.

An analytical solution for the diffusion length scale for inner and outer phase can be obtained by applying the mass balance of the surfactant concentration between the depletion region and interface. The ratio of the time scale $\tau_{\mathrm{in}}/\tau_{\mathrm{out}}$,calculated from the analytical solution, is approaching 1 when droplet radius is greater than 1mm, which verifies the observation from pendant drop experiments. $\tau_{\mathrm{in}}/\tau_{\mathrm{out}}$ starts increasing when droplet radius becomes smaller indicating an increasing diffusion boundary layer thickness for the inner phase. Until the droplet radius reaches a critical value $3h_{\mathrm{p}}$, where the boundary layer thickness is the same as the radius of the droplets, $\tau_{\mathrm{in}}/\tau_{\mathrm{out}}$ starts decreasing again with the radius. However, the predicted $\tau_{\mathrm{in}}/\tau_{\mathrm{out}}$ from the analytical solution of micro-scale droplets does not match with the experimental results. The average radius of the droplets in the microfluidic experiments are approximately $40\ \mu\mathrm{m}$, which is in the same order of the critical radius to distinguish the diffusion controlled and kinetic controlled surfactant transport, $R_C \sim 10\ \mu\mathrm{m}$, obtained by Alvarez et. al. In addition, the Peclet number for both inside and outside droplet is in the order of $O(10^3)$, further implying that the kinetic-controlled surfactant transport impacts on the IFT decaying time scale. The kinetic-controlled surfactant adsorption and desorption constant for the microscale droplets are then extracted by fitting Langmuir's equation to the dynamic IFT results.

In overall, the current work provides an insight into the fundamental understanding of size and phase dependency of dynamic IFT and surfactant transport. The results presented here inform the interfacial dynamics of droplets in bilgewater system under different conditions, which helps improve the mitigation strategies of oil-water emulsion stability. Knowing the time-dependent IFT for an interface of a given curvature and surface-to-volume ratio aids in determining the driving force for the droplets to destabilize and coalesce[8] for an emulsion of a given size distribution. In particular, the smaller the interfacial tension, the lower driving force, which leads to the reduced separation of oil from the bulk emulsion. For the smaller microscale droplets, the interface may reach the equilibrium IFT much faster than larger droplets, resulting in a more difficult-to-break emulsion. The equilibrium IFT and decaying time scale obtained in this work will potentially provide quantitative information to improve treatment operation and residence times. Information about the dynamic IFT, as well as the CMC based on IFT (not ST) measurements can also provide fundamental information on the stability of the emulsion system and guidance to determine the optimal bilgewater treatment methods, such as membrane separation, centrifugation, or other physical/chemical separation[65]. Beyond IFT itself, the rate of change of IFT with respect to any change in the droplet surface area can yield interfacial dilatational modulus.[66] This modulus is dependent on the surfactant gradient on the fluid-fluid interface and describes the response of the interface to deformation. Therefore, it is also linked to the probability of droplet coalescence and emulsion stability[67].

Future studies could incorporate the approaches of Davies isotherm to account for the charge effects from the anionic surfactant used in the current study. Else, the combined Frumkin-Davies isotherm can be applied if the interaction between the molecules at the interface needs to be considered. In addition to these isotherm models, the generalized Ward and Tordai equation for surfactant mixtures can be more appropriate for the complex systems and may yield more accurate results as compared to the current model. Still, the current work with the more simplified approach is valuable through the determination of the curvature-dependent adsorption/desorption rate constants for the surfactants used in this study. Future work will also include measuring the dynamic IFT of a wide range of diameters for both micro-scale and milli-scale droplets. In addition, using model oil and aqueous phase, such as mineral oil and DI water, can avoid any effects due to multiple chemical compositions on the dynamic IFT.

Conflicts of interest

There are no conflicts to declare.

Acknowledgements

The authors would like to thank Shweta Narayan, Athena Metaxas, Audrey Sebastian, for helping with this project. This work is performed under the support of the SERDP project WP18-1031. Portions of this work were conducted in the Minnesota Nano Center, which is supported by the National Science Foundation through the National Nano Co-ordinated Infrastructure Network (NNCI) under Award Number ECCS-1542202.

References

1 B. K. Körbahti and K. Artut, *Desalination*, 2010, **258**, 219–228.

2 I. Vyrides, E.-M. Drakou, S. Ioannou, F. Michael, G. Gatidou and A. S. Stasinakis, *J. Environ. Manage.*, 2018, **217**, 356–362.

3 A. Moslehyani, M. Mobaraki, A. M. Isloor, A. F. Ismail and M. H. D. Othman, *React. Funct. Polym.*, 2016, **101**, 28–38.

4 S. M. Emadian, M. Hosseini, M. Rahimnejad, M. H. Shahavi and B. Khoshandam, *Ecol. Eng.*, 2015, **82**, 272–275.

5 J. Church, D. M. Paynter and W. H. Lee, *Langmuir*, 2017, **33**, 9731–9739.

6 J. Church, J. G. Lundin, D. Diaz, D. Mercado, M. R. Willner, W. H. Lee and D. M. Paynter, *Sci. Total Environ.*, 2019, **691**, 981–995.

7 H. Eskandarloo, M. J. Selig and A. Abbaspourrad, *Chem. Eng. J.*, 2018, **335**, 434–442.

8 S. Narayan, D. B. Moravec, B. G. Hauser, A. J. Dallas and C. S. Dutcher, *Energy & Fuels*, 2018, **32**, 7326–7337.

9 G. Bessee and S. Hutzler, *SAE Int. J. Fuels Lubr.*, 2009, **2**, 287–293.

10 J. Wang, M. Ponting, C. Zhang, A. Olah and E. Baer, *J. Memb. Sci.*, 2017, **526**, 229–241.

11 N. J. Alvarez, L. M. Walker and S. L. Anna, *Langmuir*, 2010, **26**, 13310–13319.

12 F. Jin, R. Balasubramaniam and K. J. Stebe, *J. Adhes.*, 2004, **80**, 773–796.

13 R. Miller, E. V Aksenenko and V. B. Fainerman, *Adv. Colloid Interface Sci.*, 2017, **247**, 115–129.

14 N. J. Alvarez, L. M. Walker and S. L. Anna, *Phys. Rev. E*, 2010, **82**, 11604.

15 Q. Brosseau, J. Vrignon and J.-C. Baret, *Soft Matter*, 2014, **10**, 3066–3076.

16 Y. He, P. Yazhgur, A. Salonen and D. Langevin, *Adv. Colloid Interface Sci.*, 2015, **222**, 377–384.

17 N. J. Alvarez, D. R. Vogus, L. M. Walker and S. L. Anna, *J. Colloid Interface Sci.*, 2012, **372**, 183–191.

18 A. F. H. Ward and L. Tordai, *J. Chem. Phys.*, 1946, **14**, 453–461.

19 J. Eastoe and J. S. Dalton, *Adv. Colloid Interface Sci.*, 2000, 85, 103–144.

20 A. J. Prosser and E. I. Franses, *Colloids Surfaces A Physicochem. Eng. Asp.*, 2001, **178**, 1–40.

21 V. L. Kolev, K. D. Danov, P. A. Kralchevsky, G. Broze and A. Mehreteab, *Langmuir*, 2002, **18**, 9106–9109.

22 R. Miller, V. B. Fainerman and H. Möhwald, *J. Surfactants Deterg.*, 2002, **5**, 281–286.

23 R. Pan, J. Green and C. Maldarelli, *J. Colloid Interface Sci.*, 1998, **205**, 2, 213-230.

24 C. A. MacLeod and C. J. Radke, *Langmuir*, 1994, **10**, 3555–3566.

25 S. S. Datwani and K. J. Stebe, *Langmuir*, 2001, **17**, 4287–4296.

26 S. S. Datwani and K. J. Stebe, *J. Colloid Interface Sci.*, 1999, **219**, 282–297.

27 R. P. Borwankar and D. T. Wasan, *Chem. Eng. Sci.*, 1988, **43**, 1323–1337.

28 M. Mulqueen and D. Blankschtein, *Langmuir*, 1999, **15**, 8832–8848.

29 M. Mulqueen, K. J. Stebe and D. Blankschtein, *Langmuir*, 2001, **17**, 5196–5207.

30 C. H. Chang, N. H. L. Wang and E. I. Franses, *Colloids and Surfaces*, 1992, **62**, 321–332.

31 J. K. Ferri and K. J. Stebe, *Adv. Colloid Interface Sci.*, 2000, **85**, 61–97.

32 B. Riechers, F. Maes, E. Akoury, B. Semin, P. Gruner and J.-C. Baret, *Proc. Natl. Acad. Sci.*, 2016, **113**, 11465–11470.

33 A. Yeung, T. Dabros and J. Masliyah, *J. Colloid Interface Sci.*, 1998, **208**, 241–247.

34 H. Liu and Y. Zhang, *J. Appl. Phys.*, 2009, **106**, 34906.

35 X.-B. Li, F.-C. Li, J.-C. Yang, H. Kinoshita, M. Oishi and M. Oshima, *Chem. Eng. Sci.*, 2012, **69**, 340–351.

36 P. Garstecki, M. J. Fuerstman, H. A. Stone and G. M. Whitesides, *Lab Chip*, 2006, **6**, 437–446.

37 G. F. Christopher and S. L. Anna, *J. Phys. D. Appl. Phys.*, 2007, **40**, R319–R336.

38 M. DE MENECH, P. GARSTECKI, F. JOUSSE and H. A. STONE, *J. Fluid Mech.*, 2008, **595**, 141–161.

39 A. R. Metcalf, S. Narayan and C. S. Dutcher, *Aerosol Sci. Technol.*, 2018, **52**, 310–329.

40 Y. Xia and G. M. Whitesides, *Annu. Rev. Mater. Sci.*, 1998, **28**, 153–184.

41 D. Qin, Y. Xia and G. M. Whitesides, *Nat. Protoc.*, 2010, **5**, 491.

42 J. C. McDonald and G. M. Whitesides, *Acc. Chem. Res.*, 2002, **35**, 491–499.

43 J. Zhou, D. A. Khodakov, A V Ellis and N. H. Voelcker, *Electrophoresis*, 2012, **33**, 89–104.

44 M. Yao and J. Fang, *J. Micromechanics Microengineering*, 2012, **22**, 025012.

45 T. Trantidou, Y. Elani, E. Parsons and O. Ces, *Microsystems &Amp; Nanoeng.*, 2017, **3**, 16091.

46 L. G. Rigat-Brugarolas, A. Homs-Corbera and J. Samitier, *RSC Adv.*, 2015, **5**, 7423–7425.

47 D. Maji, S. K. Lahiri and S. Das, *Surf. Interface Anal.*, 2012, **44**, 62–69.

48 S. H. Tan, N.-T. Nguyen, Y. C. Chua and T. G. Kang, *Biomicrofluidics*, 2010, **4**, 32204.

49 J. D. Martin and S. D. Hudson, *New J. Phys.*, 2009, **11**, 115005.

50 A. Nadim and H. A. Stone, *Stud. Appl. Math.*, 1991, **85**, 53–73.

51 S. D. Hudson, *Rheol Acta*, 2010, **49**, 237–243.

52 G. I. Taylor, *Proc. R. Soc. London. Ser. A, Contain. Pap. a Math. Phys. Character*, 1934, **146**, 501–523.

53 S. D. Hudson, J. T. Cabral, W. J. Goodrum, K. L. Beers and E. J. Amis, *Appl. Phys. Lett.*, 2005, **87**, 81905.

54 J. T. Cabral and S. D. Hudson, *Lab Chip*, 2006, **6**, 427–436.

55 A. R. Metcalf, H. C. Boyer and C. S. Dutcher, *Environ. Sci. Technol.*, 2016, **50**, 1251–1259.

56 C. Cowan-Ellsberry, S. Belanger, P. Dorn, S. Dyer, D. Mcavoy, H. Sanderson, D. Versteeg, D. Ferrer and K. Stanton, *Crit. Rev. Environ. Sci. Technol.*, 2014, **44**, 1893–1993.

57 R. Pan, J. Green and C. Maldarelli, *J. Colloid Interface Sci.*, 1998, **205**, 213–230.

58 C. Dong, C.-T. Hsu, C.-Y. Chiu and S.-Y. Lin, *Langmuir*, 2000, **16**, 4573–4580.

59 A. Zdziennicka and B. Jańczuk, *J. Colloid Interface Sci.*, 2010, **350**, 568–576.

60 N. J. Alvarez, W. Lee, L. M. Walker and S. L. Anna, *J. Colloid Interface Sci.*, 2011, **355**, 231–236.

61 C. H. Chang and E. I. Franses, *Colloids Surfaces A Physicochem. Eng. Asp.*, 1995, **100**, 1–45.

62 K. D. Danov, P. A. Kralchevsky, N. D. Denkov, K. P. Ananthapadmanabhan and A. Lips, *Adv. Colloid Interface Sci.*, 2006, **119**, 1–16.

63 K. D. Danov, P. A. Kralchevsky, N. D. Denkov, K. P. Ananthapadmanabhan and A. Lips, *Adv. Colloid Interface Sci.*, 2006, **119**, 17–33.

64 S. Bochner De Araujo, M. Merola, D. Vlassopoulos and G. G. Fuller, *Langmuir*, 2017, **33**, 10501–10510.

65 J. Church, J. G. Lundin, D. Diaz, D. Mercado, M. R. Willner, W. H. Lee and D. M. Paynter, *Sci. Total Environ.*, 2019, **691**, 981–995.

66 A. P. Kotula and S. L. Anna, *J. Rheol. (N. Y. N. Y).*, 2015, **59**, 85–117.

67 A. K. Malhotra and D. T. Wasan, *Chem. Eng. Commun.*, 1987, **55**, 95–128.